Microporous and Mesoporous Materials 266 (2018) 75–82

Contents lists available at ScienceDirect

Microporous and Mesoporous Materials

journal homepage: www.elsevier.com/locate/micromeso

Effects of SiO_2-forming additive on polysiloxane derived SiOC ceramics

Donald Erb, Kathy Lu*

Department of Materials Science and Engineering, Virginia Tech, Blacksburg, VA, 24061, USA

ARTICLE INFO

Keywords:
Silicon oxycarbide
Polymer derived ceramics
Pore
Specific surface area
Voronoi diagram

ABSTRACT

Novel ultrahigh surface area materials are highly desired for demanding applications such as high temperature catalysts, electrodes, and harsh environment sensors. In-situ conversion of tetraethyl orthosilicate (TEOS) into SiO_2 and its incorporation into silicon oxycarbide (SiOC) ceramics during polysiloxane ceramization are investigated by crosslinking TEOS within a polysiloxane matrix and introducing water vapor during pyrolysis. The effects of the TEOS-derived SiO_2 on the thermophysical properties, phase development, and the resulting porous SiOC are investigated. The SiOC with 10 wt% TEOS within the crosslinked polymer creates the highest specific surface area of ~2100 m^2/g with an average pore size of ~2 nm. The specific surface area and pore size distribution are correlated with the theoretical results from Voronoi diagram simulation and an idealized model calculation.

1. Introduction

Silicon oxycarbide (SiOC) is a polymer derived ceramic through which polysiloxane polymer precursors undergo thermal decomposition and bond rearrangement, resulting in amorphous or nanocrystalline ceramics (or a mixture of both) with a wide range of tailorable properties, such as high temperature stability, oxidation resistance, and electrical conductivity, depending on the pyrolysis temperature and specific composition [1–3].

In general, porous SiOC can be fabricated with a wide range of pore sizes using several different processing routes before, during, or after pyrolysis, such as by using sacrificial fillers, sacrificial templating, direct foaming, polymer precursor phase separation, and selective removal of phases after pyrolysis [4–7]. However, to create ultrahigh surface areas, only controlled phase separation during pyrolysis and selective phase removal after pyrolysis at the nanocluster level are feasible means, which can create pores with less than 10 nm sizes and very narrow distributions.

Phase separation in an evolving SiOC system can be introduced using two different methods. The first is through phase separation of the polymer precursors during crosslinking. When two or more immiscible polymers co-exist as liquid precursors, they will separate and form two distinct phases after crosslinking. One of the phases can then evaporate after cross-linking or decompose during pyrolysis, leaving behind pores. The SiOC ceramics created with this method have high specific surface areas at temperatures around 600 °C. However, the specific surface area may decrease as the temperature increases due to the sintering of transient pores [4,8]. The second method is by controlling phase evolution within SiOC during pyrolysis. At temperatures above 1100 °C, the amorphous SiOC phase separates into free carbon and amorphous SiO_2 nanodomains along with SiOC units of different stoichiometry. Pyrolysis to even higher temperatures, e.g., greater than 1250 °C, leads to further phase separation and thus more carbon and SiO_2, as well as nanocrystalline SiC [9,10]. From this point forward, the pyrolysis temperature can significantly influence the phase separation and the separated domain sizes. After pyrolysis, certain ceramic phases can be etched away, such as using hydrofluoric acid (HF) to remove SiO_2 nanodomains or chlorine gas to remove SiC nanocrystals, leaving behind single nanometer pores [1,11]. Therefore, nucleation and growth, concentration, and size of different ceramic phases within SiOC are critical factors influencing the final porous SiOC materials.

SiO_2 nanodomain sizes in SiOC are related to both system chemistry and processing conditions. From ~1000 °C to ~1250 °C, SiO_2 nanoclusters are the main separated phase along with turbostratic carbon. In this temperature range, the SiO_2 nanodomains largely remain amorphous but the correspondingly sizes increase with pyrolysis temperature. Saha et al. [12] reported that the size of the SiO_2 nanodomains is also dependent on the Si:O elemental ratio of the SiOC, with larger Si:O ratios producing smaller domain sizes. The effect of polymer precursor molecular structure on the resulting SiO_2 domain size is shown by comparing a linear polymer, polyhydridomethylsiloxane (PHMS), and a cyclic polymer, 1,3,5,7-tetramethyl-1,3,5,7-tetracyclotetrasiloxane (TMTS), having the same chemical composition. After pyrolysis at 1400 °C, the PHMS sample has only amorphous SiO_2,

* Corresponding author. 213 Holden Hall, Virginia Tech, Blacksburg, VA, 24061, USA.
E-mail address: klu@vt.edu (K. Lu).

https://doi.org/10.1016/j.micromeso.2018.02.034
Received 8 November 2017; Received in revised form 30 January 2018; Accepted 25 February 2018
Available online 02 March 2018
1387-1811/ © 2018 Elsevier Inc. All rights reserved.

while the TMTS sample contains both amorphous and crystalline SiO_2 [13,14]. After etching both samples with HF, the PHMS sample has a higher micropore volume compared to the TMTS sample due to the presence of smaller SiO_2 domains [13].

SiO_2 formation in SiOC can also be influenced by pyrolysis atmosphere, such as by introducing reactive species into the pyrolysis gas, e.g., H_2 or H_2O [15–18]. Our previous work demonstrated that injecting water vapor during the temperature range at which precursor bond (chain) breaking occurs results in a dramatic decrease in carbon precipitation and an increase in Si-O-Si bond formation [7,17,18]. The resulting SiOC sample pyrolyzed at 1300 °C after HF etching has a specific surface area of 2391.6 m^2/g, much greater than the specific surface area of the sample pyrolyzed in Ar at the same temperature, 630.41 m^2/g [18]. Liang et al. [15] investigated water vapor injection effects on the chemistry and atomic bonding of SiOC from 500 °C to 1000 °C. The samples pyrolyzed in the water vapor atmosphere have only about half the carbon content compared to the samples pyrolyzed in Ar, resulting in a reduction of SiC_4 and SiC_2O_2 structural units and an increase in SiO_4 units.

Additives can be introduced into the polymer precursor to further react with the pyrolysis atmosphere. By adding 10 wt% tetraethylorthosilicate (TEOS), a water reactive molecule, to a commercial polysiloxane and then pyrolyzing in an Ar + H_2O atmosphere, the specific surface area of the SiOC after HF etching increases from 1108.5 m^2/g for the base polysiloxane to 1953.9 m^2/g for the sample with TEOS. Additionally, the average pore size of the 10 wt% TEOS sample is 1.66 nm, less than the 3.03 nm pore size of the polysiloxane sample [19]. However, the evolution of the TEOS during the polymer to ceramic transformation or its effect on the phase separation within SiOC is yet unknown; it is unclear whether the TEOS would interact with the SiOC system to form SiO_2 or experience SiO_2 nucleation and growth independently.

Understanding and creating highly porous SiOC is of high interest for fundamental understanding, such as addressing the questions related to SiO_2 nucleation and growth as well as molecular interactions of different precursors. Porous SiOC also has many exciting applications, e.g., electrodes in lithium ion batteries, catalyst supports, thermal barriers, gas separation membranes, and lightweight components [20–22]. In this work, micro- and meso-porous SiOC ceramics are fabricated through the addition of TEOS to a polysiloxane precursor and then pyrolysis in a water vapor-containing atmosphere. After pyrolysis, SiO_2 nanoclusters are etched with a HF solution to create single nanometer pores. The effects of the additive amount and pyrolysis temperature on the resulting thermophysical properties, phase evolution, specific surface area, and pores of the SiOC ceramic are studied.

2. Experimental procedures

A commercial polysiloxane (PSO, $[-Si(C_5H_6)_2O-]_3[-Si(CH_3)(H)O-]_2[-Si(CH_3)(CH=CH_2)O-]_2$, SPR-684, Starfire Systems, Inc. Gelest Inc. Schenectady, NY) was chosen as the base precursor, tetraethyl orthosilicate (TEOS, $Si(OC_2H_5)_4$, Sigma-Aldrich, St. Louis, MO) was used as the additive, and 2.1–2.4% platinum-divinyltetramethyldisiloxane complex in xylene (Pt catalyst, Gelest Inc. Morrisville, PA) was used as the catalyst.

First, solutions with PSO and either 0, 10, 20, 30, or 40 wt% TEOS were sonicated for 10 min and then mixed in a high energy mill (SPEX 8000M Mixer/Mill, SPEX SamplePrep, Metuchen, NJ) for 10 min to form a homogeneous mixture. Next, the Pt catalyst (1 wt% relative to PSO) was added, the mixtures were mixed again in the high energy ball mill for 5 min, and then poured into aluminum foil molds. The mixtures were placed into a vacuum chamber and vacuumed for 10 min at 200 Torr to remove any bubbles in the solutions. After that, the molds were put in an oven to crosslink at 50 °C for 12 h and then at 120 °C for 6 h. All solutions initially had slightly greater than the listed weight of TEOS added in order to account for the evaporation of the additive during processing, so the actual content of TEOS added was 11, 22, 32, and 43 wt% for the nominal 10, 20, 30, and 40 wt% samples, respectively. The samples were also sealed during the curing process to prevent additional loss of TEOS. The samples designated as 100PSO corresponded to the pure PSO sample; the samples with the additive were labelled as XTEOS, where X was from 10 wt% to 40 wt%, depending on the TEOS amount.

For pyrolysis, the crosslinked materials were first cut and polished into circular pieces roughly 10 mm in diameter and 2 mm in thickness. Next, the samples were placed into a zirconia crucible, covered on both sides with graphite mats in order to reduce friction during shrinkage and prevent warping [23,24], and put into a tube furnace (1730-20 Horizontal Tube Furnace, CM Furnaces Inc. Bloomfield, NJ). With an Ar flow rate of approximately 500 std cm^3/min, the samples were heated up to 1100 °C, 1300 °C, or 1400 °C at a rate of 1 °C/min, held for 2 h, cooled to 400 °C with a rate of 1 °C/min, and finally cooled to 50 °C with a rate of 2 °C/min. During heating from 500°C to 700 °C, the Ar gas was bubbled through water at 60 °C, giving a gas flow with a Ar:H_2O molar ratio of approximately 5:1.

Etching of the bulk SiOC samples after pyrolysis was done using a HF solution (20 wt% HF in water). The HF solution was magnetically stirred at room temperature until there was no significant mass loss, taking approximately 4 days (supplement Table S2). The SiOC samples were then rinsed with deionized water and dried at 120 °C. Bulk density of the samples after etching was determined geometrically by dividing the mass after etching by the volume of the samples measured using the image analysis software ImageJ [25].

Ceramic yield was calculated by measuring the mass of the samples before and after the pyrolysis. The apparent density after pyrolysis was measured using the Archimedes method with water as the medium [26]. The phase compositions of the pyrolyzed samples were analyzed in an X'Pert PRO diffractometer (PANalytical B.V. EA Almelo, the Netherlands) with Cu Kα radiation. The JCPDS reference cards used to identify the crystalline phases were 00-039-1425 for SiO_2, 00-029-1129 for SiC, and 01-075-1621 for C. The chemical bonding was evaluated using Fourier Transform Infrared Spectroscopy (FT-IR) (Nicolet 8700 with Pike GladiATR attachment, Thermo Scientific, Waltham, MA) between 500 and 4000 cm^{-1} wavenumber with a resolution of 4 cm^{-1} and averaged between 64 scans. The specific surface area, pore size distribution, and specific pore volume of the pyrolyzed samples were evaluated using nitrogen adsorption at 77 K with a Quantachrome Autosorb-1 (Quantachrome Instrumenets, Boynton Beach, FL), and the samples were degassed before testing for 3 h at 300 °C. The relative pressure range used to calculate the specific surface area using the BET method was determined based on the procedure proposed by Rouquerol et al. [27]; the calculated specific surface area should be considered as the "BET-equivalent specific surface area" due to the complications of applying the BET theory to microporous materials. The pore size distribution and specific pore volume were derived by applying the Non Local Density Functional Theory (NLDFT) model for N_2 adsorption on carbon with cylindrical pores to the adsorption branch of the data [28]. Assuming cylindrical pores, the average pore size was estimated using $4000V_p/SSA$, where V_p is the specific pore volume, and SSA is the specific surface area [29].

Modeling of the SiOC microstructure after etching was computed using Voronoi software (Rhinoceros 5.0, Robert McNeel and Associates, Seattle, WA). First, a three dimensional Voronoi tessellation model was created, and spheres were then placed within the center of each Voronoi cell to represent pores (or SiO_2 nanodomains before etching) within the SiOC matrix. The pore size distributions used in the model were generated by first fitting the experimental pore size distributions from nitrogen adsorption with log-normal distributions (see supplement Fig. S3). Random pore diameters corresponding to the fitted distributions were then generated using Mathematica software (Mathematica 11.0, Wolfram, Champaign, IL). After the generation of the cubes containing the Voronoi cells and corresponding pores, images along the

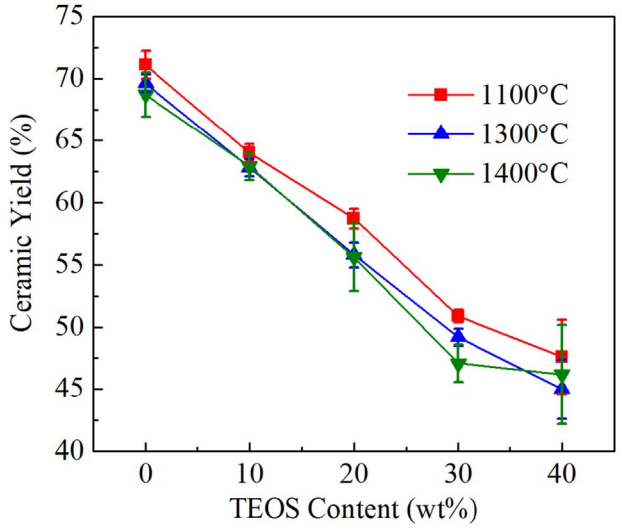

Fig. 1. Ceramic yield of the SiOC samples after pyrolysis at different temperatures.

length of the cube were taken in order to produce 3D reconstructions of the samples (Amira 5.4.1, FEI, Hillsboro, OR), giving the specific surface area and pore volume of the simulated SiOC microstructures after the HF etching.

3. Results and discussion

3.1. Thermophysical properties

The ceramic yields of the SiOC samples are shown in Fig. 1 as a function of the TEOS content at different pyrolysis temperatures. After pyrolysis at 1100 °C, the ceramic yield decreases from 71.1% to 47.6% with the TEOS content increase from 0 to 40 wt%. The samples pyrolyzed at 1400 °C also change similarly, even though in general the ceramic yield is lower, from 68.7% to 46.2% at 0–40 wt% TEOS addition. The yield results at 1300 °C pyrolysis temperatures are in-between those at the other two pyrolysis temperatures with no significant difference. For all the samples, pyrolysis temperature causes only a slight decrease in the ceramic yield from 1100 °C to 1300 °C. From 1300 °C to 1400 °C, there is no significant yield change. Increasing the TEOS content causes a continuous decrease in the ceramic yield at all pyrolysis temperatures. This decrease can be attributed to the evaporation of TEOS from the sample at low pyrolysis temperatures, the hydrolysis and condensation of the TEOS molecules during the water vapor injection between 500 °C and 700 °C, and the evaporative species loss through Eqs. (1)–(9) (Section 3.2). At pyrolysis temperatures 1300 °C and above, mass loss can also occur based on Eqs. (10) and (11) (Section 3.2).

As understood from our earlier work [6,18], at > 1100 °C pyrolysis temperature, there is continuous phase separation of SiO_2 and crystallization of SiC. Based on Eqs. (10) and (11) to be discussed later, the phase separation process may or may not induce mass loss due to the formation of CO gas. If the phase evolution follows Eq. (10), the mass of the SiOC sample should remain unchanged during the phase separation. If the phase evolution follows Eq. (11), the mass of the SiOC sample should decrease. However, for the system in this work, the mass loss is minimal, suggesting that the formation of SiC is very limited, as to be discussed later (Section 3.2).

The apparent densities of the samples after pyrolysis between 1100 °C and 1400 °C vary from 1.62 ± 0.02 g/cm^3 to 1.87 ± 0.03 g/cm^3. There is no consistent trend or significant change with the pyrolysis temperature (see supplement Table S1). For PSO, 10TEOS, and 20TEOS, the density ranges from 1.76 ± 0.06 g/cm^3 to 1.88 ± 0.01 g/cm^3. The 30TEOS and 40TEOS samples have slightly lower densities ranging between 1.62 ± 0.02 g/cm^3 to 1.83 ± 0.02 g/cm^3. The lower densities for the 30TEOS and 40TEOS samples is likely due to the more extensive evaporation of the TEOS molecules during the early stages of pyrolysis leaving behind macropores in the samples rather than a fundamental difference in the polymer to ceramic conversion, considering that lowering the PSO content in the polymer would cause a decrease in the carbon content in the ceramic, which should increase the density of the SiOC in this work [24]. The measured density values for the samples in this study are in good agreement with those obtained from previous studies with the same PSO precursor (1.6 g/cm^3- 1.8 g/cm^3) [18,19,24].

3.2. Phase evolution

To understand the effect of the TEOS addition on the chemical bonding of the system, the FT-IR spectra of the crosslinked polymers are shown in Fig. 2. In Fig. 2(a), all the crosslinked samples show sharp peaks, corresponding to the phenyl (695, 715, 740, 1430, 3000-3070 cm^{-1}) and methyl (1260 cm^{-1}) side groups in the PSO polymer. The broad peak between 1000 and 1100 cm^{-1} wavenumbers can be assigned to Si-O-Si [30]. With the addition of TEOS, the peaks at 785, 1170, 1298, 1390, 1440, 2890, 2929, and 2975 cm^{-1} increase, indicative of increasing amounts of TEOS [31]. Fig. 2(b) compares the C-H vibration at 2955 cm^{-1}, found only in PSO, and 2975 cm^{-1}, found only in TEOS, as the TEOS content in the polymer is increased. The continuous decrease of the 2955 cm^{-1} peak and increase of the 2975 cm^{-1} peak indicate that the concentration of TEOS within the crosslinked polymers increases from 10TEOS to 40TEOS, consistent with the designed composition changes.

Before the pyrolysis temperature reaches 1100 °C, the fundamental phase evolution process in the studied system can be understood by

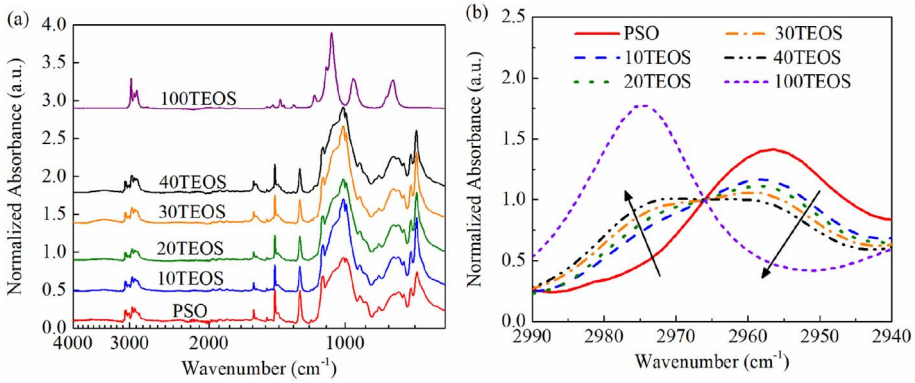

Fig. 2. (a) Normalized FT-IR spectra for the PSO-TEOS precursors after crosslinking along with pure PSO and pure TEOS. (b) The spectra from (a) normalized to 2966 cm^{-1} to illustrate the effect of increasing TEOS content.

examining the mass loss. With the presence of water vapor between 500 °C and 700 °C, the polymer to ceramic transformation occurs with the following reactions [15,17].

$$Si\text{-}H + H_2O \rightarrow Si\text{-}OH + H_2\uparrow \quad (1)$$

$$Si\text{-}CH_3 + H_2O \rightarrow Si\text{-}OH + CH_4\uparrow \quad (2)$$

$$Si\text{-}CH_2\text{-}Si + H_2O \rightarrow Si\text{-}OH + Si\text{-}CH_3 \quad (3)$$

$$Si\text{-}CH_2\text{-}CH_2\text{-}Si + 2H_2O \rightarrow 2Si\text{-}OH + C_2H_6\uparrow \quad (4)$$

$$Si\text{-}CH{=}CH_2 + H_2O \rightarrow Si\text{-}OH + C_2H_4\uparrow \quad (5)$$

$$Si\text{-}C_6H_5 + H_2O \rightarrow Si\text{-}OH + C_6H_6\uparrow \quad (6)$$

Further, TEOS hydrolyzes following Eq. (7):

$$Si\text{-}O\text{-}C_2H_5 + H_2O \rightarrow Si\text{-}OH + C_2H_5OH \quad (7)$$

The Si-OH bonds can then condense to form Si-O-Si bonds:

$$Si\text{-}OH + Si\text{-}OH \rightarrow Si\text{-}O\text{-}Si + H_2O\uparrow \quad (8)$$

In addition, free carbon that precipitates between 500 °C and 700 °C may also oxidize following the reaction [15,18,32].

$$C_{free} + H_2O \rightarrow H_2\uparrow + CO\uparrow \quad (9)$$

According to Eqs. (1)–(9), water vapor facilitates Si-O bond formation while reducing Si-C bonds and consuming free carbon. Fig. 3(b) clearly reflects this when compared to samples pyrolyzed without water vapor injection [18]. The prominent formation of SiO_2 compared to SiC for all of the samples is due to the decrease of Si-C bonds in the water vapor environment [15].

Fig. 3(a) shows the XRD patterns of the SiOC samples pyrolyzed in the Ar + H_2O atmosphere at 1100 °C. All the samples show an amorphous SiO_2 halo centered around ~23° [29]. In addition, all the samples exhibit a peak at ~44°, which corresponds to the (100) plane of turbostratic carbon [29,33–35]. The lack of any crystalline peaks for SiO_2 shows that the TEOS-derived SiO_2 remains amorphous rather than crystallizing. Due to the broad amorphous peak characteristic of SiOC ceramics pyrolyzed at temperatures below ~1200 °C, the onset of major phase separation, the amorphous SiO_2 within the samples cannot be distinguished from the SiOC matrix, and the samples show no differences in Fig. 3(a) [6,18,36].

Increasing the pyrolysis temperature to 1400 °C (Fig. 3(b)) results in the samples showing more obvious SiO_2 (22°) and C peaks (44°), as well as weak SiC peaks at 35.6°, 60°, and 72°. The presence of the SiO_2, SiC, and carbon diffraction peaks for the samples pyrolyzed at 1400 °C occurs due to the phase separation of SiOC, as well as the carbothermal reduction of SiO_2 into SiC. The main reactions that produce SiO_2, SiC, and C within the ceramics are given by the following reactions [10,37].

$$2SiOC \rightarrow SiO_2(amorphous) + SiC(\beta) + C \quad (10)$$

$$SiO_2(amorphous) + 3C \rightarrow SiC(\beta) + 2CO\uparrow \quad (11)$$

Higher TEOS contents lead to slightly more obvious phase peaks (C peak at 44° as well as weak SiC peaks at 35.6°, 60°, and 72°). Overall, there is no major peak difference.

The XRD patterns for the SiOC samples pyrolyzed at 1100 °C and 1400 °C after the HF etching are shown in Fig. 4(a) and (b), respectively. Dotted lines show the original positions of the amorphous hump before etching. For the 1100 °C pyrolyzed samples (Fig. 4(a)), the XRD patterns show a slightly lower halo with a right peak shift, indicating the removal of the amorphous SiO_2 phase. However, the difference between Figs. 3(a) and 4(a) is fairly small, again confirming that the SiO_2 phase separation is insignificant at 1100 °C. In Fig. 4(b), however, the samples no longer show the amorphous SiO_2 hump around 23°; rather, the center of the diffused peak shifts to approximately 24.5°, due to the contributions of the SiOC, residual SiO_2, and turbostratic carbon, which has a peak at approximately 26° from the (002) plane [34,35,38]. The SiC peaks and the C peaks all become much more visible. This means a rather large amount of amorphous SiO_2 phase has been etched away. The etching of the SiO_2 nanodomains by the HF solution is well understood as [18].

$$SiO_2 + 6HF \rightarrow H_2SiF_6 + 2H_2O \quad (12)$$

In addition, a new diffraction peak emerges after etching the 1400 °C samples, at approximately 78°, which corresponds to the (110) plane of carbon [35].

Fig. 4(c) directly compares the peaking splitting results from Figs. 3(b) and Fig. 4(b) at ~22–25 °C. Before the HF etching (Fig. 3(a)), there are three deconvoluted halos/peaks corresponding to SiO_2 (21.6°), SiOC (22.7°), and C (26.0°). The dominance of the SiO_2 halo is obvious with the highest intensity. After the HF etching, only the SiOC halo (22.7°) and the C peak are present with the peak splitting. This comparison directly shows the removal of SiO_2 due to the HF etching.

3.3. Specific surface areas and pores

Nitrogen adsorption was not conducted on the samples pyrolyzed at 1100 °C due to the low mass loss from etching and thus the insignificant amount of pores from the SiO_2 removal. All the samples pyrolyzed at 1400 °C have similar specific surface areas, specific pore volumes, and pore sizes (Table S3 and Fig. S1, supplement), meaning that the SiO_2 nanodomains have grown to similar sizes due to more extensive phase separation, which agrees with the high specific pore volume and larger pore size in Table S3. Thus, Fig. 5 only shows the nitrogen adsorption curves for the samples pyrolyzed at 1300 °C after the HF etching. All the samples show a large adsorption volume at low relative pressures, followed by a relative constant adsorption volume at higher relative pressures; this adsorption behavior corresponds to the Type I isotherm, according to the IUPAC classification, which indicates that the samples are prominently microporous with only monolayer adsorption [39]. In

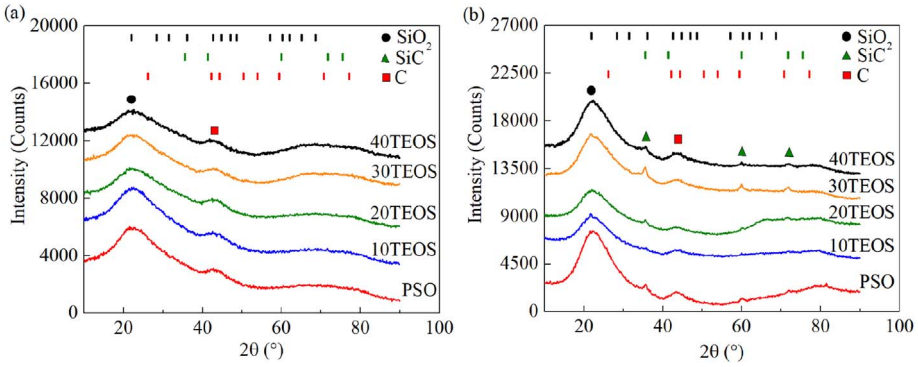

Fig. 3. XRD patterns for different polymer precursors after pyrolysis at (a) 1100 °C and (b) 1400 °C.

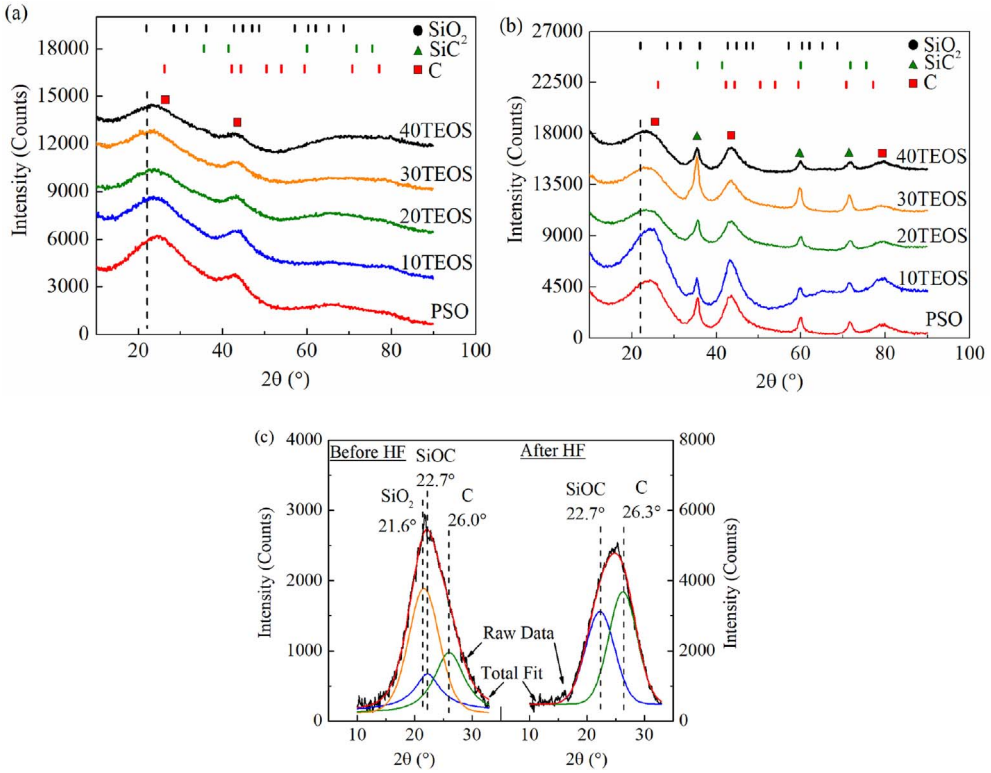

Fig. 4. XRD patterns after HF etching of the SiOC samples pyrolyzed at (a) 1100 °C and (b) 1400 °C, and (c) a comparison of peak fitting before and after etching.

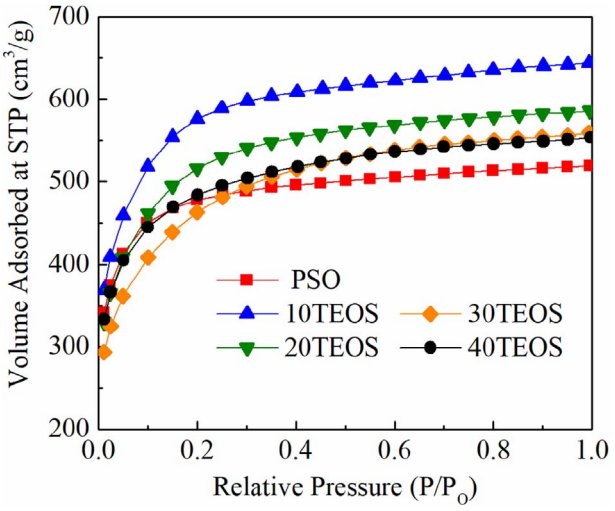

Fig. 5. Nitrogen adsorption curves for the samples pyrolyzed at 1300 °C after etching.

detail, the PSO sample has an adsorbed gas volume of 519 cm^3/g at a relative pressure ≈1. The 10TEOS sample, however, has the highest adsorbed gas volume of 644 cm^3/g. When the TEOS content increases to 20, 30, and 40 wt%, the adsorbed gas volume decreases from 586 cm^3/g and then stabilizes at approximately 553 cm^3/g. This means that the phase separated SiO_2 in the SiOC has a maximum at 10 wt% TEOS; higher TEOS content is not conducive for the desired SiO_2 formation.

The specific surface area, specific pore volume, and average pore size after etching for all of the samples pyrolyzed at 1300 °C are summarized in Table 1. The addition of 10 wt% TEOS creates more surface area, with the specific surface area increasing from 1812.1 m^2/g to 2107.2 m^2/g from the pure PSO to the 10TEOS. This means that water vapor pyrolysis can facilitate the hydrolysis and condensation of TEOS into SiO_2 during the pyrolysis following Eqs. (7) and (8) and thus increase the SiO_2 content in the SiOC. With additional TEOS content,

Table 1
Nitrogen adsorption results for the SiOC ceramics pyrolyzed at 1300 °C after the HF etching.

sample	BET-equivalent apparent specific surface area (m^2/g)	NLDFT specific surface area (m^2/g)	specific pore volume (cm^3/g)
PSO	1812.1	2091.1	0.76
10TEOS	2107.2	2200.6	0.99
20TEOS	1876.1	1962.6	0.89
30TEOS	1666.9	1745.4	0.86
40TEOS	1794.9	2024.1	0.85

however, the specific surface area decreases to 1876.1 m^2/g for 20TEOS, 1666.9 m^2/g for 30TEOS, and 1794.9 m^2/g for 40TEOS. This means that the amount and distribution of SiO_2 nanoclusters in the SiOC also plays an important role in the specific surface area value, as to be discussed in Section 3.4.

The specific pore volume follows the same general trend as the specific surface area, with the specific pore volume initially increasing from 0.764 m^3/g for PSO to 0.99 cm^3/g for 10TEOS. Further increase in the TEOS content from 20 to 40 wt% has little effect on the specific pore volume, instead it decreases from 0.89 cm^3/g for 20TEOS to 0.85 cm^3/g for 40TEOS.

The pore size distributions obtained from the NLDFT fitting for the samples pyrolyzed at 1300 °C are shown in Fig. 6 (a comparison between the experimental isotherms and the fitted NLDFT isotherms is shown in the supplement Fig. S2). For the PSO sample, the pore size distribution shows a peak at ~1.6 nm and then some broad distribution at larger pore sizes. With the addition of 10 wt% TEOS, the pore size distribution has a wider and higher peak at 1.6–1.8 nm. In addition, a small peak at 3.5 nm emerges, and the pore size distribution becomes wider with a higher volume of pores between 2 and 4 nm. With an increase to 20TEOS, the peaks at 1.6 nm and 1.8 nm shrink and the peak at 3.5 nm slightly grows. Increasing the TEOS content for the 30TEOS sample causes further decrease in the volume of small pores and pronounced increase in pores around 3.5 nm. Interestingly, the 40TEOS

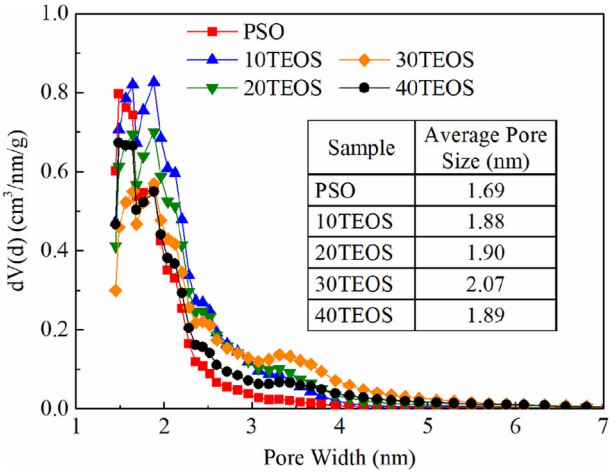

Sample	Average Pore Size (nm)
PSO	1.69
10TEOS	1.88
20TEOS	1.90
30TEOS	2.07
40TEOS	1.89

Fig. 6. Pore size distributions for the samples pyrolyzed at 1300 °C.

sample shows a similar pore size distribution as PSO, with only one peak at 1.6 nm and a much smaller peak at 3.5 nm. It should also be noticed that the 10TEOS sample has the highest peak height at 1.6–1.8 nm pore sizes. The other composition samples all have lower peak height, especially for higher TEOS samples. This means that the higher TEOS samples may contain fewer pores. Overall, for the 10TEOS sample, the specific pore volume is highest, and the pore size is rather small. Correspondingly, the specific surface area is highest.

3.4. SiOC microstructure understanding

Considering the ceramic yields, XRD patterns, and nitrogen adsorption results, the effect of TEOS-derived SiO_2 on the formation of SiO_2 within SiOC can be understood as follows. During the pyrolysis, for the pure PSO, polymer decomposition and SiOC phase separation lead to SiO_2 nanocluster formation, as shown in Fig. 7(a). For the TEOS-containing PSO, the SiO_2 domains in the SiOC matrix during pyrolysis come from two sources: the SiOC matrix and the TEOS hydrolysis. Initially, when TEOS is added into PSO, it disperses. At low TEOS content (Fig. 7(b)), even though some TEOS clusters might be present, they are rather small due to the similar nature of hydrophobicity. When the SiO_2 nanoclusters derived from the aggregated TEOS clusters are small enough to be comparable with the PSO phase separation induced SiO_2 nanoclusters, these SiO_2 domains co-exist with limited merging, and thus generate very large surface areas after etching. Such a sample would contain more small and independent pores (Fig. 7(b)), consistent with Fig. 6. This is the case for the 10 wt% TEOS sample, the TEOS-derived SiO_2 is relatively independent of the SiO_2 which initially forms from the phase separation of SiOC. The system has a specific pore volume of 0.99 cm^3/g, much greater than that of the PSO (0.76 cm^3/g). However, as the TEOS content increases (Fig. 7(c)), TEOS molecule aggregation increases. When the TEOS content is high, the resultant SiO_2 clusters are either large to start with due to the TEOS aggregation, or small SiO_2 nanodomains are so close that they merge and grow into larger sizes, either among themselves or with the PSO derived SiO_2 clusters. As a result, the pore sizes increase and the specific surface area decreases. In this work, at > 10 wt% content of TEOS, the results in Figs. 5 and 6 show that the TEOS-derived SiO_2 nanodomains can no longer remain sufficiently separate; instead, they merge with other SiO_2 domains derived from either the TEOS or the SiOC matrix, creating more pores between 3 and 4 nm without forming more pores at ~1.6 nm. The merging of the SiO_2 domains can be considered analogous to phase separation of the SiOC matrix; the ceramic yield and the etching results confirm this hypothesis. The higher TEOS content samples contain increasing content of SiC (Figs. 3(b) and Fig. 4(b)), which must have occurred through phase separation of the SiOC matrix (Eq. (10)) because the carbothermal reduction of SiO_2 into SiC (Eq. (11)) would have caused a significant decrease in the ceramic yield between 1100 °C and 1400 °C, a lower etching mass loss, and smaller specific pore volume, none of which were observed. Thus, it can be concluded that the initial SiO_2 nuclei size is roughly 1.6 nm, and the SiO_2 size after phase separation and further growth is approximately 3.5 nm. This growth of the SiO_2 phase after phase separation is supported by the nitrogen adsorption results for all of the samples pyrolyzed at 1400 °C (supplement Fig. S1), in which all samples show a decrease in the amount of pores of < 2 nm in favor of a larger amount of pores at ~3.5 nm in size. In addition, due to the drop in carbon within the SiOC, the SiO_2 clusters are more prone to evaporation into SiO gas, further decreasing the utility of the TEOS-derived SiO_2. A qualitative illustration of the TEOS effect on the SiO_2 nanocluster formation in SiOC is shown in Fig. 7.

A more thorough three dimensional understanding of the SiOC microstructure after the HF etching was computed according to a Voronoi model, with the SiO_2 nanodomains (or pores after etching) as spheres within the center of each Voronoi cell. The size distribution of the spheres within the Voronoi cells was based on the nitrogen adsorption experimental results, and a comparison between the generated values for the pore diameters and the experimental data is shown for each of the samples in Fig. S2(a)-(e) (supplement).

In this work, 50 Voronoi cells with the superimposed pores are created within a cube with a side length l, defined in order to match with the specific pore volume of the samples:

$$l = \left(\frac{50\pi\, d^3}{6\, V_p\, \rho_b} \right)^{1/3} \tag{13}$$

where d is the average pore diameter in nm, as listed in Fig. 6, V_p is the specific pore volume, in cm^3/g, as listed in Table 1, and ρ_b is the

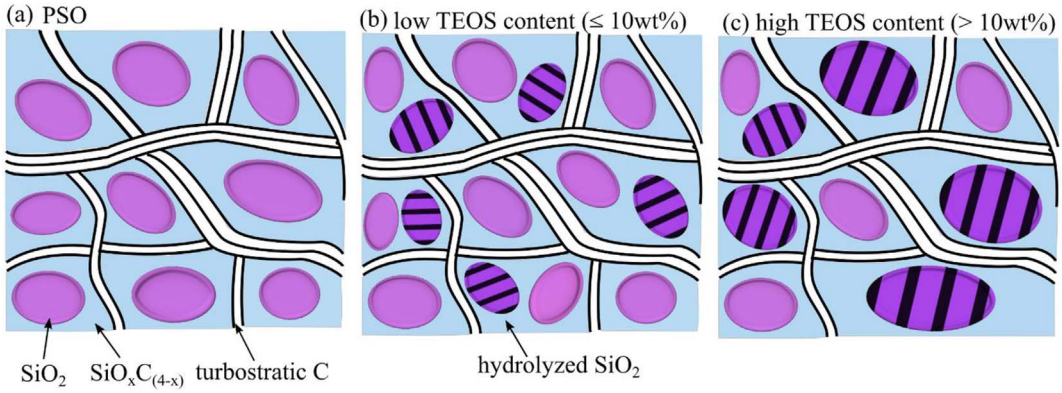

Fig. 7. Illustration of the TEOS effect on the SiO_2 nanocluster formation in SiOC.

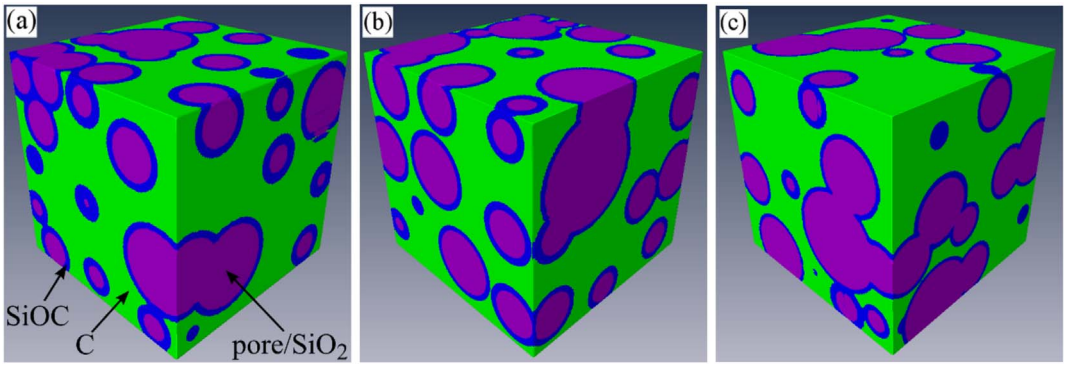

Fig. 8. Simulated SiOC after the HF etching for the (a) PSO, (b) 10TEOS, and (c) 30TEOS samples pyrolyzed at 1300 °C. The purple color represents pores (the original SiO_2 nanoclusters), the blue color represents SiOC, and the green color represents C. (For interpretation of the references to color in this figure legend, the reader is referred to the Web version of this article.)

measured bulk density of the samples after etching in g/cm^3. They are 0.61, 0.58, 0.58, 0.57, and 0.60 g/cm^3 from the pure PSO sample to the 40TEOS sample.

The 3D images of the etched PSO, 10TEOS, and 30TEOS samples obtained from the Voronoi model are shown in Fig. 8. The PSO sample has more connected pores, the 10TEOS sample has a large number of independent pores, and the 30TEOS sample has a higher number of connected pores, matching the earlier hypotheses based on the experimental results. Suitable amount of TEOS addition creates more small and separated SiO_2 nanoclusters of similar size to that of the PSO phase separated SiO_2 nanoclusters.

From the 3D structures in Fig. 8, the surface area S_{sim} with units of nm^2 is converted to specific surface area SSA_{sim} with a unit of m^2/g, using:

$$SSA_{sim} = \frac{1000\ S_{sim}}{\rho_b V_{sim}} \tag{14}$$

where V_{sim} is the total volume of the 3D structure of the sample in nm^3. Likewise, the porosity from the 3D reconstruction P_{sim} is used to calculate the specific pore volume $V_{p,sim}$ with a unit of cm^3/g according to:

$$V_{p,sim} = \frac{P_{sim}}{\rho_b} \tag{15}$$

The results for the specific surface area and specific pore volume of the simulated samples are compared to the experimental results in Fig. 9(a) and (b), respectively. For the specific surface area, the simulated models for all of the samples give slightly higher values than those obtained experimentally, although all of the samples except for the PSO show only a minor shift from the expected values, demonstrating that the model is consistent for all of the samples. The poorer correlation for the PSO samples is likely due to the less than desired left branch of the pore size distribution curve (see supplement Fig. S4), which causes deviation during the curve fitting and discretization of different sizes of pores. Likewise, the specific pore volumes from the model are consistently yet only slightly higher than their experimental values. The higher values from the simulation than those from the experiments are believed to be due to the inaccessibility of the small as well as closed pores during the BET measurements, which effectively lowers the measured specific surface area and pore volume values. The results in Fig. 9 (a) and (b) demonstrate that representation of the SiOC matrix using a Voronoi spatial distribution gives reasonable results, allowing the visualization of the distribution of SiO_2 domains within the SiOC matrix.

To estimate the theoretical specific surface area of the SiOC matrix after etching, a simple spherical core-shell hexagonal packing model can be created as shown in the insert of Fig. 10, in which one spherical SiO_2 domain is surrounded by different layers of turbostratic carbon. As seen, the number of graphene sheets wrapping around the pores has a tremendous effect on the specific surface area. When the turbostratic carbon layer is 1, the specific surface area ranges from 1780 to 2332 m^2/g. However, when the turbostratic carbon layers are 2, the specific surface area changes from 770 to 819 m^2/g, a substantial decrease. When the turbostratic carbon layers are 3, 4, and 5, the specific surface areas are ~450, 280, 200 m^2/g, showing continuous and significant decreases. It should also be noticed that the diameter of the pores, from 1 nm to 5 nm, also has an observable effect on the specific surface area when the carbon layer is 1, with larger size pores causing a continuous increase of the specific surface area. When the number of the carbon layers is 2 or higher, the pore size effect on the specific surface area is negligible. It should be clarified that this observation only applies to single size pores, not to be confused with the pores with different size distributions shown in Fig. 6. Overall, a thin carbon layer around the pores is essential to achieving high specific surface areas.

For our studied system, the specific surface area ranges from 1667

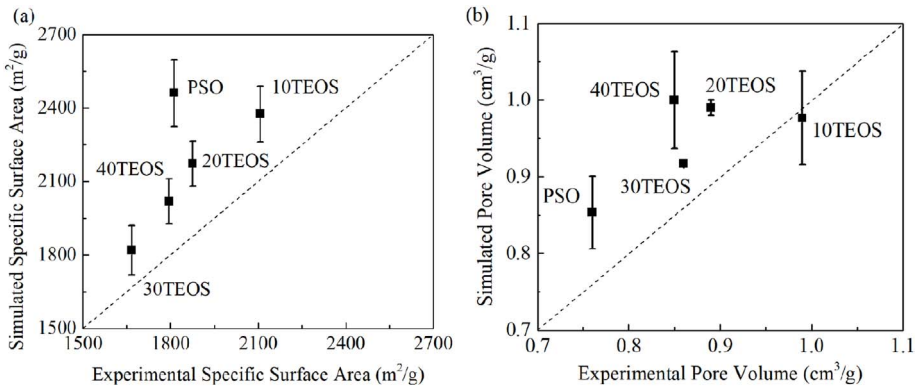

Fig. 9. Comparison between the experimental and simulated (a) specific surface areas and (b) specific pore volumes. The dashed line indicates what a perfect agreement should be between the simulations and experiments (with a slope of 1).

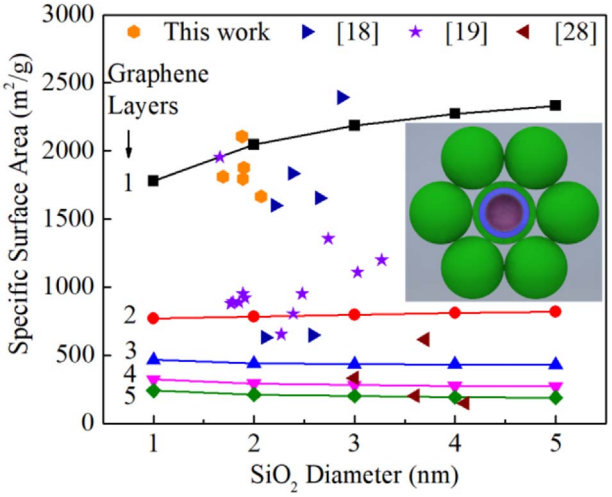

Fig. 10. Specific surface area calculation assuming one pore is surrounded by different layers of turbostratic carbon and the hollow shell units pack regularly. The experimental data from this work and other studies are also indicated by different markers.

to 2107.2 m^2/g, very close to and understandably slightly lower than these theorized values, as shown in Fig. 10. The specific surface areas obtained from our earlier work and another group are also indicated on Fig. 10 by different symbols. It proves that very thin layers of turbostratic carbon and SiO_2 nanoclusters are intimately intergrown during the pyrolysis.

For the pore volumes, using the spherical packing model with 2 layers of graphitic carbon and 1.88 nm pore size (for the 10TEOS sample), the projected specific pore volume is still much higher at 2.24 cm^3/g. Other samples have similar specific pore volumes because of the similar pore sizes in Fig. 6. The difference between the idealized model and the actual samples can be related to many factors such as pore shape, accessibility of the pores, the composition and thus the density of the matrix, etc.

Nonetheless, based on this theoretical idealization, the challenge in creating high specific surface area materials is creating small size and uniform pores with a thin shell and keeping them from merging, which would require great processing condition control.

4. Conclusions

The in-situ conversion of TEOS into SiO_2 and its incorporation within SiOC ceramics is investigated by crosslinking TEOS within a polysiloxane matrix and introducing water vapor during pyrolysis. The effect of the TEOS-derived SiO_2 on the phase development within the SiOC is studied. With the optimal TEOS addition (10 wt%) within the crosslinked polymer, SiO_2 forms from the hydrolysis and condensation of the TEOS with the water vapor atmosphere, independently of the SiO_2 formed from the phase separation of the SiOC matrix. These independent SiO_2 nuclei can be etched away, creating a higher number of ~2 nm size pores, an increase in the specific surface area (up to ~2100 m^2/g), and higher specific pore volume (~1 cm^3/g). The fundamental microstructural evolution is further studied using Voronoi cell modeling and theoretical calculation. Consistent results with the experiments are demonstrated.

Notes

The authors declare no competing financial interest.

Conflicts of interest

The authors declare that they have no conflict of interest.

Acknowledgements

We acknowledge the financial support from National Science Foundation under grant number CMMI-1634325.

Appendix A. Supplementary data

Supplementary data related to this article can be found at http://dx.doi.org/10.1016/j.micromeso.2018.02.034.

References

[1] P. Colombo, G. Mera, R. Riedel, G.D. Soraru, J. Am. Ceram. Soc. 93 (2010) 1805–1837.
[2] K. Lu, D. Erb, M. Liu, J. Mater. Chem. C 4 (2016) 1829–1837.
[3] K. Lu, D. Erb, M.Y. Liu, J. Mater. Sci. 51 (2016) 10166–10177.
[4] Y. Blum, G.D. Soraru, A.P. Ramaswamy, D. Hui, S.M. Carturan, J. Am. Ceram. Soc. 96 (2013) 2785–2792.
[5] P. Colombo, J. Eur. Ceram. Soc. 28 (2008) 1389–1395.
[6] J.K. Li, K. Lu, T.S. Lin, F.Y. Shen, J. Am. Ceram. Soc. 98 (2015) 1753–1761.
[7] K. Lu, Mater. Sci. Eng. R 97 (2015) 23–49.
[8] J.L. Wan, M.J. Gasch, A.K. Mukherjee, J. Am. Ceram. Soc. 84 (2001) 2165–2169.
[9] H. Brequel, J. Parmentier, G.D. Soraru, L. Schiffini, S. Enzo, Nanostruct. Mater. 11 (1999) 721–731.
[10] A. Saha, R. Raj, J. Am. Ceram. Soc. 90 (2007) 578–583.
[11] L. Biasetto, R. Pena-Alonso, G.D. Soraru, P. Colombo, Adv. Appl. Ceram 107 (2008) 106–110.
[12] A. Saha, R. Raj, D.L. Williamson, J. Am. Ceram. Soc. 89 (2006) 2188–2195.
[13] P. Dibandjo, S. Dire, F. Babonneau, G.D. Soraru, Glass Technol. Eur. J. Glass Sci. Technol. A 49 (2008) 175–178.
[14] P. Dibandjo, S. Dire, F. Babonneau, G.D. Soraru, J. Non-Cryst. Solids 356 (2010) 132–140.
[15] T. Liang, Y.-L. Li, D. Su, H.-B. Du, J. Eur. Ceram. Soc. 30 (2010) 2677–2682.
[16] M. Narisawa, K. Terauds, R. Raj, Y. Kawamoto, T. Matsui, A. Iwase, Scripta Mater. 69 (2013) 602–605.
[17] K. Lu, J. Li, J. Eur. Ceram. Soc. 36 (2016) 411–422.
[18] J.K. Li, K. Lu, J. Am. Ceram. Soc. 98 (2015) 2357–2365.
[19] D. Erb, K. Lu, J. Eur. Ceram. Soc. 37 (2017) 4547–4557.
[20] Y. Juttke, H. Richter, I. Voigt, R.M. Prasad, M.S. Bazarjani, A. Gurlo, R. Riedel, Chem. Eng. Trans. 32 (2013) 1891–1896.
[21] P. Dibandjo, M. Graczyk-Zajac, R. Riedel, V.S. Pradeep, G.D. Soraru, J. Eur. Ceram. Soc. 32 (2012) 2495–2503.
[22] V.S. Pradeep, D.G. Ayana, M. Graczyk-Zajac, G.D. Soraru, R. Riedel, Electrochim. Acta 157 (2015) 41–45.
[23] N. Janakiraman, F. Aldinger, J. Eur. Ceram. Soc. 29 (2009) 163–173.
[24] S. Martinez-Crespiera, E. Ionescu, H.J. Kleebe, R. Riedel, J. Eur. Ceram. Soc. 31 (2011) 913–919.
[25] C.A. Schneider, W.S. Rasband, K.W. Eliceiri, Nat. Methods 9 (2012) 671–675.
[26] ASTM C20-00, Standard Test Methods for Apparent Porosity, Water Absorption, Apparent Specific Gravity, and Bulk Density of Burned Refractory Brick and Shapes by Boiling Water, ASTM International, West Conshohocken, PA, 2015.
[27] J. Rouquerol, P. Llewellyn, F. Rouquerol, Stud. Surf. Sci. Catal. 160 (2006) 49–56.
[28] P.I. Ravikovitch, A.V. Neimark, Colloids Surf. A 187 (2001) 11–21.
[29] R. Peña-Alonso, G.D. Sorarù, R. Raj, J. Am. Ceram. Soc. 89 (2006) 2473–2480.
[30] M. Halim, C. Hudaya, A.Y. Kim, J.K. Lee, J. Mater. Chem. A 4 (2016) 2651–2656.
[31] M.I. Tejedor-Tejedor, L. Paredes, M.A. Anderson, Chem. Mater. 10 (1998) 3410–3421.
[32] G. Tobias, L.D. Shao, C.G. Salzmann, Y. Huh, M.L.H. Green, J. Phys. Chem. B 110 (2006) 22318–22322.
[33] A.M. Wilson, G. Zank, K. Eguchi, W. Xing, B. Yates, J.R. Dahn, Chem. Mater. 9 (1997) 2139–2144.
[34] R. Pena-Alonso, G. Mariotto, C. Gervais, F. Babonneau, G.D. Soraru, Chem. Mater. 19 (2007) 5694–5702.
[35] Z.Q. Li, C.J. Lu, Z.P. Xia, Y. Zhou, Z. Luo, Carbon 45 (2007) 1686–1695.
[36] T. Rouxel, G. Massouras, G.D. Soraru, J. Sol. Gel Sci. Technol. 14 (1999) 87–94.
[37] H.J. Kleebe, C. Turquat, G.D. Soraru, J. Am. Ceram. Soc. 84 (2001) 1073–1080.
[38] G.D. Soraru, R. Pena-Alonso, M. Leoni, Micropor. Mesopor. Mater. 172 (2013) 125–130.
[39] K.S.W. Sing, Pure Appl. Chem. 54 (1982) 2201–2218.